PHYSICAL REVIEW B **82**, 014104 (2010)

Structure and energetics of ferroelectric domain walls in $LiNbO_3$ from atomic-level simulations

Donghwa Lee (이동화),[1] Haixuan Xu (徐海譞),[1] Volkmar Dierolf,[2] Venkatraman Gopalan,[3] and Simon R. Phillpot[1,*]
[1]*Department of Materials Science and Engineering, University of Florida, Gainesville, Florida 32611, USA*
[2]*Department of Physics, Lehigh University, Bethlehem, Pennsylvania 18015, USA*
[3]*Department of Materials Science and Engineering, Pennsylvania State University, University Park, Pennsylvania 16802, USA*

(Received 6 April 2010; revised manuscript received 10 June 2010; published 8 July 2010)

Atomistic simulations with empirical potentials and density-functional theory calculations are used to characterize the structure, energetics, and ferroelectric properties of domain walls in $LiNbO_3$. The two methods yield similar polarization patterns and atomic structures at the domain walls. The structure of the domain wall on the mixed anion-cation planes is very different from that of the domain wall on planes of alternating cations and anions. The breaking of the uniaxial symmetry of the ferroelectric phase by the domain walls leads to nonuniaxial contributions to the polarization in the domain-wall region. In particular, a polarization component parallel to the domain walls leads to a Bloch-type rotation while a polarization component normal to the domain walls leads to Néel-type rotation. The polarization profiles at the domain walls are fitted to Ginzburg-Landau-Devonshire theory. The comparison of energetics at equilibrium and at transition states yields estimates of the energy barrier heights for domain-wall motion.

DOI: 10.1103/PhysRevB.82.014104 PACS number(s): 77.80.Dj, 31.15.E−, 75.60.Ch, 31.15.bu

I. INTRODUCTION

Lithium niobate ($LiNbO_3$) is a ferroelectric material with a high spontaneous polarization (~70 $\mu C/cm^2$), high Curie temperature (~1480 K), excellent piezoelectric, pyroelectric, and nonlinear optical properties.[1,2] Because of its unique ferroelectric and nonlinear optical properties, $LiNbO_3$ has many applications in optoelectronics,[3] nonlinear optics,[4] and microelectromechanical devices.[5] In the high-temperature paraelectric state, $LiNbO_3$ has a trigonal ($R\bar{3}c$) structure.[6] It becomes ferroelectric at the Curie temperature, loses its inversion symmetry along the c axis, resulting in space group $R3c$. Figure 1(a) shows schematic side views of the paraelectric and ferroelectric (up and down polarization) phases. Since all of the ion displacements associated with the ferroelectricity are parallel to the c axis (i.e., along [0001]), the paraelectric and ferroelectric phases look identical in the top view, Fig. 1(b). The polarization state can be switched by the simultaneous movement of Li ions through an oxygen plane and the displacement of the Nb atoms within an oxygen cage; there is also a small amount of motion of the oxygen ions during this switching process. Molecular-dynamics (MD) simulation previously showed that the phase transition is displacive in nature for the Nb atoms in the oxygen cage and order disorder in nature for the movement of the Li atom through the oxygen plane.[7]

Gopalan *et al.*[8] identified two crystallographically different domain walls between domains of opposite polarization. As discussed in detail below, an X wall lies parallel to a mixed anion-cation plane while a Y wall lies parallel to alternating planes of cations only and anions only. They derived a relationship between the domain-wall width and energy based on Ginzburg-Landau-Devonshire (GLD) theory.[9] However, the detailed atomic structure and energetics of these domain walls has not been determined. The objective of this work is, therefore, to characterize the structure and energetics of these domain walls. The approach we will take is atomic-level simulation with empirical potentials, validated against electronic-structure calculations at the level of density-functional theory (DFT).

II. SIMULATION METHODOLOGY

All the DFT (Refs. 10 and 11) calculations are performed with the Vienna *ab initio* simulation Package (VASP).[12,13] The projected augmented wave (PAW) (Ref. 14) pseudopotential within the generalized gradient approximation (GGA) (Ref. 15) is used to evaluate the exchange and correlation interactions. The outmost shells of each ion, $2s^1$ on Li, $4p^6 4d^4 5s^1$ on Nb, and $2s^2 2p^4$ on O, are considered as active valence states for the interactions and are treated explicitly; the energy cutoff for the plane waves is 400 eV.[16] A conjugate gradient and quasi-Newton algorithm are used for the ionic

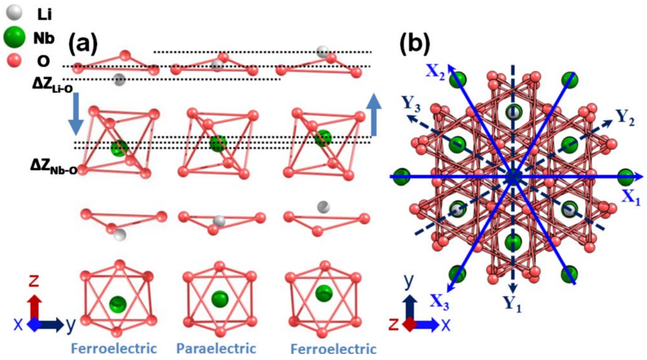

FIG. 1. (Color online) Structure of $LiNbO_3$. (a) Edge view of down polarization (left), paraelectric (center), and up polarization (right) states. (b) Planar view of (0001) plane. The up polarization is obtained when the Nb atoms shift up from the octahedra centers and the Li atoms sit above their oxygen planes. Correspondingly, down polarization is obtained when the Nb atoms are shifted down and the Li atoms sit below the oxygen planes. Three equivalent hexagonal axes are drawn X_1, X_2, X_3 and Y_1, Y_2, Y_3, with X_1 and Y_1 parallel to the Cartesian x and y axes.

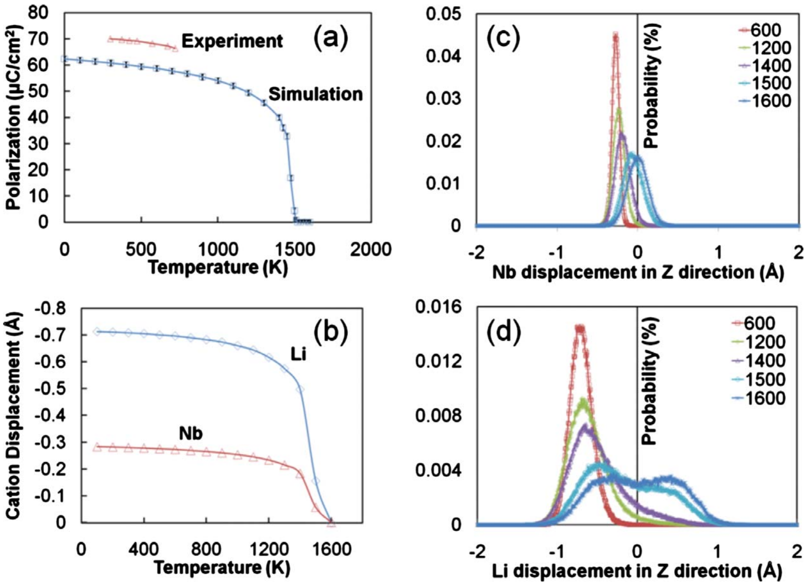

FIG. 2. (Color online) (a) Temperature dependence of polarization of $\mathrm{LiNbO_3}$ from experiment and MD calculation; (b) temperature dependence of averaged displacement of Li and Nb ions from an oxygen plane and the center of the oxygen cage; (c) probability distribution profiles for (c) $\Delta Z_{\text{Nb-O}}$ and (d) $\Delta Z_{\text{Li-O}}$ for various temperatures.

relaxation.[17] The force criterion for complete ionic relaxation is 0.0001 eV/Å. The residual minimization method direct inversion in the iterative subspace algorithm,[18] which optimizes several individual energy bands at the same time, is used for electronic energy minimization. The pseudopotential and methodologies used here are the same as used previously in studies of intrinsic defects in $\mathrm{LiNbO_3}$.[19]

Electronic-structure calculations generally give the highest materials fidelity among available simulation methods. Unfortunately they are not suitable for the systematic study of these domain walls because the computational load for the system sizes required is prohibitively high. For example, eight unit cells for $\mathrm{LiNbO_3}$, contains 240 atoms and 1440 electrons, is large for a DFT study. However, we are able to perform benchmark DFT calculations in which the domain walls are particularly close together, against which, to compare our atomic-level simulations with empirical potentials. As we shall see, the two methods show good agreement.

Most of the results presented here come from atomic-level simulation with empirical potentials. The maximum system size for the study includes $36\times4\times3$ unit cells (12960 atoms). This large size, considerably beyond the capabilities of DFT calculations, allows domain walls to be characterized with essentially no interactions with a neighboring domain wall. The interatomic potential used was developed by Jackson *et al.*[20] This potential contains four terms: a short-range interaction, a long-range electrostatic interaction, an interaction between core and shell, and a three-body interaction. The short-range interactions are described by the Buckingham potential whose functional form is

$$V_{Buck}(r) = A\exp(-r/\rho) - C/r^6, \tag{1}$$

where r is the distance between two different ion species, and A, ρ, and C are potential parameters. Three different interatomic interactions, Li-O, Nb-O, and O-O are included in the Buckingham potentials. The interatomic interactions are cut off using a shifted force method at a distance of 10.2 Å, which corresponds to twice the lattice parameter along [1000]. The electronic polarizability of the ions is captured in a shell model which describes each ion as a core consisting of the nucleus and inner electrons, and a shell of valence electron; the core and shell are connected by a harmonic spring,

$$V(\omega) = \frac{1}{2}k_2\omega^2, \tag{2}$$

where ω is the core-shell displacement and k_2 is the harmonic spring constants. The core and shell carry partial charges, the sum of which is the full ionic charge of each atom species. The positions of the cores and shells are determined in a fully dynamic manner with fictional masses of 10% of the mass of the individual ions are assigned to the shells.

The core and shell of each ion interact with the cores and shells of other ions through Coulombic interactions,

$$V_{ij}^{Coulomb}(r) = \frac{q_i q_j}{4\pi\varepsilon_0 r_{ij}}, \tag{3}$$

where r_{ij} is the distance between the core or shell position of two species whose charges are q_i and q_j. The direct summation method of Wolf *et al.*[21] is used for the calculation of the Coulombic interactions.

A three-body harmonic O-Nb-O is also applied,

$$V_{ijk} = \frac{1}{2}k_\theta(\theta-\theta_0)^2, \tag{4}$$

where θ and $\theta_0=90°$ are the actual and ideal angle between O-Nb-O and k_θ is the three-body harmonic constant.

The ferroelectric polarization of $\mathrm{LiNbO_3}$ can be understood in terms of the electronic polarizations associated with the core-shell interactions, the displacements of Li and Nb ions from the high symmetry positions of the paraelectric phase, and the associated small oxygen displacements. Figure 2(a) shows the temperature dependence of the polarization as determined with the Jackson potential. The polarization decreases quite gradually up to 1400 K, above which it

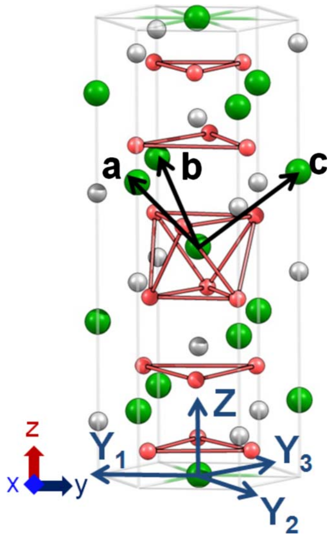

FIG. 3. (Color online) Crystallographic direction of rhombohedral axes (middle) and hexagonal axes (bottom) in a unit cell of ferroelectric $LiNbO_3$. The Cartesian axes are given at the bottom left of the figure.

rapidly drops to zero at 1500–1510 K, which we take as an estimate of the Curie temperature for this potential. This value is in good agreement with the experimental Curie temperature of 1483 K.[6] This result is also supported by an analysis of the distribution profile of the displacements of the Nb and Li atoms from the centers of the oxygen octahedra and from the oxygen planes. Well below the Curie temperature, the main effect of the increased temperature is a broadening of the distribution of cation positions about their displaced values with only a small decrease in polarization. At temperatures above 1400 K, there is a significant shift of the cations to positions that are symmetric relative to the oxygen sublattice, with an associated significantly decreased polarization. Figure 2(b) shows the average displacements of the Li and Nb ions from their crystallographically expected sites, both of which decrease to zero at the Curie temperature. We see that the Nb displays displacive dynamics, Fig. 2(c), while the Li ions show order-disorder behavior, Fig. 2(d), consistent with the results previously obtained with the Tomlinson potential.[22] These results differ from the previous results using the Tomlinson potential,[7] which showed that the Nb displacements went to zero well below the Curie temperature; this effect is not seen for this potential.

III. CRYSTALLOGRAPHY OF $LiNbO_3$

Before we discuss the domain-wall structure, it is necessary to understand the crystallography of $LiNbO_3$ in some detail. This section provides the necessary background. To understand the crystallography and properties of $LiNbO_3$, it is necessary to use three distinct coordinate systems: rhombohedral, hexagonal, and Cartesian coordinates, see Fig. 3. The Cartesian coordinates are denoted as x, y, and z; the rhombohedral coordinates are denoted as a, b, and c; the hexagonal coordinates are denoted as Y_1, Y_2, Y_3, and Z. The rhombohedral coordinates can be represented as $a=\sqrt{3}/2x-1/2y+1/3z$, $b=-\sqrt{3}/2x-1/2y+1/3z$, and $c=y+1/3z$. The hexagonal coordinates can be represented as $Y_1=-y$, $Y_2=\sqrt{3}/2x+1/2y$, $Y_3=-\sqrt{3}/2x+1/2$, and $Z=z$.

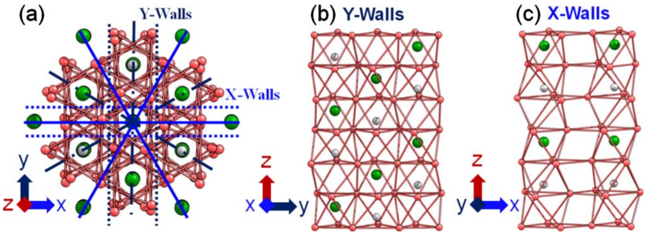

FIG. 4. (Color online) (a) Schematic view parallel to the (0001) plane showing two structurally distinct domain-wall structures; (b) planar structure of Y wall on $(11\bar{2}0)$ plane; and (c) planar structure of X wall on $(10\bar{1}0)$ plane.

The domain walls in $LiNbO_3$ separate regions with polarizations in the $+z$ [0001] and $-z$ $[000\bar{1}]$ directions. Scrymgeour *et al.*[9] determined that two different crystallographic planes can define the domain wall. In Fig. 4(a) the X walls and Y wall are projected onto the (0001) plane. The Y wall lies parallel to c-glide planes, thus containing only cations or anions, but not both. The X wall lies perpendicular to c-glide planes, and thus contains both cation and anions. Figures 4(b) and 4(c) show slices through these domain walls on one side of the wall, parallel to $(11\bar{2}0)$ for the Y wall and parallel to $(10\bar{1}0)$ for the X wall. The "up" polarization is obtained when the Nb atoms shift up from the octahedra centers and the Li atoms sits above their oxygen planes. Correspondingly, "down" polarization is obtained when the Nb atoms are shifted down and the Li atoms sit below the oxygen planes.

In the paraelectric $R\bar{3}c$ (No. 167) state, the Li and Nb ions occupy 6a and 6b Wyckoff positions, respectively, while the oxygen ions occupy 18e Wyckoff positions. While the 6a and 6b site positions are fully defined by the crystallographic tables,[23] the positions of the 18e oxygen sites are in addition characterized but a positional parameter X_O, which defines the displacements of each oxygen ion along its associated hexagonal axis, the precise value of X_O being different in different $R\bar{3}c$ systems. Neutron powder-diffraction studies have determined the positional parameter for $LiNbO_3$ to be $X_O=0.0591-0.0607$.[24] Previous DFT studies yielded $X_O=0.036$ (Ref. 25) and 0.049 (Ref. 26) in two different local-density approximation (LDA) calculations and $X_O=0.048$ (Ref. 27) in a GGA calculation. Our DFT study gives $X_O=0.039$ which lies within the same range. In agreement with a previous empirical study,[20] our simulations with empirical potentials yield $X_O=0.034$, which is somewhat smaller than the experimental values, but very similar to the DFT values.

The crystallography of the ferroelectric phase is more complicated. On losing inversion symmetry along the Z direction during the phase transition to the ferroelectric state, the space group drops to $R3c$ (No. 161). In this structure, the Li and Nb ions both sit at 6a Wyckoff positions; the oxygen ions occupy the 18b positions. X-ray diffraction studies[28] yield a positional parameter for Li of $Z_{Li}=0.283$ for up polarization state and $Z_{Li}=0.217$ for down polarization states,

TABLE I. Comparison of positional parameters of $LiNbO_3$ between empirical calculations, DFT calculations, and experimental data. PW is Perdew and Wang, PBE is Perdew, Burke and Ernzerhof. For the empirical study, the two different values correspond to 0 K (upper) and at 293 K (lower; in the parenthesis). The 293 K values represent the average values from molecular-dynamics simulation. We are not able to stabilize the paraelectric phase at 293 K using molecular-dynamics simulation.

	Lattice parameter						
	a (Å)	c (Å)	$X_{O,para}$	$Z_{\mathrm{Li},ferro}$	u	v	w
Experiment (Refs. 24, 28, and 30)	5.148	13.863	0.0591–0.0607	0.283	0.0492	0.0113	0.0186
LDA(PW) (Ref. 27)	5.067	13.721	0.036–0.049	0.285	0.0427	0.0125	0.0183
GGA(PBE) (Ref. 27)	5.200	13.873	0.048	0.282	0.0479	0.0097	0.0199
Empirical (Ref. 20)	5.156 (5.187)	13.683 (13.710)	0.034 (0.053)	0.352 (0.288)	0.0525 (0.0563)	0.0310 (0.0294)	−0.0495 (0.0133)
GGA(PAW) (present)	5.132	13.884	0.039	0.282	0.0388	0.0128	0.0207
Empirical (present)	5.169 (5.185)	13.685 (13.738)	0.034	0.283 (0.281)	0.0527 (0.0504)	0.0308 (0.0313)	0.0208 (0.0207)

which correspond to displacements of $\Delta Z = \pm 0.033$ from the positions in the paraelectric phase; the DFT and empirical simulations yield almost identical values. In characterizing the oxygen displacements, it is important to distinguish between the Cartesian coordinates and the hexagonal coordinates, the latter being more useful for understanding the in-plane displacements. In hexagonal coordinates, the crystallographic positions of the oxygen ions in the ferroelectric state are characterized as (u, $1/3+v$, and $1/12-w$) for up polarization state and ($u-v$, $1/3-v$, and $1/12+w$) for down polarization.[29] An x-ray study[28,30] determined $(u,v,w)=(0.0492,0.0113,0.0186)$, see Table I. Values obtained from a more detailed crystallographic analysis,[24] from DFT,[27] and from simulations with the same empirical potential as we are using[20] yielded similar magnitudes. Our DFT and empirical calculations yield results consistent with the published values. The difference in oxygen position between up and down polarization is (Δv, $2\Delta v$, and $2\Delta w$). Because the X and Y directions are at 120° to each other, the two polarization states actually have the same Cartesian x coordinate, but different y coordinate. Because of the threefold rotation symmetry, the oxygen ions move along three equivalent Y directions, one of which is aligned to be parallel to the Cartesian y axis.

Because it is easier to understand the structure in the rhombohedral unit cell, Fig. 5 shows the structure along the rhombohedral [001] direction (corresponding to the $[42\bar{6}\bar{1}]$ direction in the hexagonal coordinate system). In this direction, and in the [100] and [010] directions, the alternating oxygen octahedra tilt in opposite directions with tilting angle ω. This in-plane displacement tilting can be expressed as $a^-a^-a^-$ with $\omega=24.1°$, using Glazer's notation for perovskite systems.[31]

As a result of this tilting in three spatial directions, there are six distinct oxygen layers along the z direction.[32] For up polarization state, the three bottom oxygen layers rotate counterclockwise about the z axis while the three top oxygen layers rotate clockwise, see Fig. 6(a); this six-oxygen layer pattern repeats. The rotation angle between the first and second oxygen layers is slightly different from the angle between the second and third oxygen layers. The three upper oxygen layers rotate in the opposite direction. In the bulk, these antiphase rotations cancel in both the x and y directions, leading to a net zero in-plane polarization. The down polarization shows corresponding displacements. Although the rotation angles between each layer are different from those in the up polarization state, the cancellation of the clockwise rotation of the upper three oxygen layers and the counterclockwise rotation of the bottom three oxygen layers again leads to net zero in-plane polarization.

Because the in-plane positions of the oxygen ions differ in the up and down directions, when the polarization is flipped from up to down, the positions of the oxygen ions change along one of the three equivalent hexagonal directions. Thus, the three different sets of six oxygen ions can be denoted as O1, O2, and O3 and their corresponding hexagonal axes as Y_1, Y_2, and Y_3. The arrows in Figs. 6(b) and 6(c) represent the directions of the displacements of the three types of oxygen ions when the system switches from up to down polarization. As we shall see, this complex crystallography of the single crystal has a profound effect on the structure and properties of the domain walls.

IV. DOMAIN WALLS

Every Y wall lies parallel to one of the Y axes; every X wall lies parallel to one of the X axes, symmetrically between two of the Y axes. For the Y wall parallel to the Y_1 axis, see Fig. 6(b), we can expect the O1 oxygen ions to be displaced parallel to the wall (i.e., along the Y_1 axis), and the O2 and O3 ions to be displaced along the Y_2 and Y_3 axes at $\mp 120°$ to the domain wall.

Because, the X walls lie along planes at 30° to the Y walls, they lie perpendicular to one of the Y axes [Fig. 6(c)]. For the X wall plane perpendicular to Y_2 axis, as shown in Fig. 6(c), the O2 ions mainly displace parallel to the Y_2 axis, i.e., perpendicular to the domain wall. By contrast the O1 and O3 displace mainly at ±30° from the X wall.

As we will see, because of their different crystallographies, the two domain walls show different atomic structures

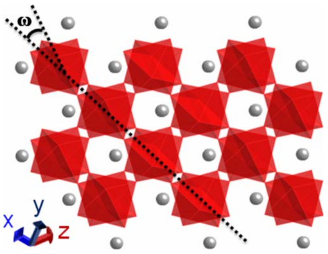

FIG. 5. (Color online) [001] projection of the rhombohedral structure. Alternating oxygen octahedra tilt in opposite directions with angle $\omega = \pm 24.1°$.

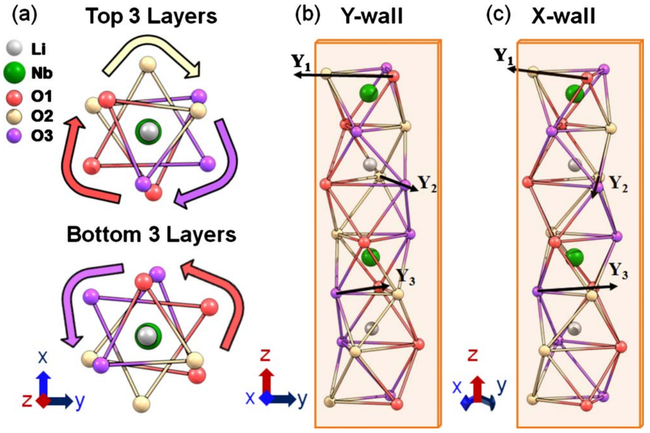

FIG. 6. (Color online) Schematic view of (a) Y_1, Y_2, and Y_3 axis along with three oxygen ions, O1, O2, and O3. (b) Crystallographic direction of Y_1, Y_2, and Y_3 axes parallel to the Y wall in the $y-z$ plane. (c) Crystallographic direction of Y_1, Y_2, and Y_3 axes parallel to X wall, i.e., parallel to an $x-z$ plane and at a 30° angle to a $y-z$ plane. The top oxygen layer of Figs. 6(b) and 6(c) is a duplicate of the bottom oxygen layer.

and different patterns of polarization in the domain-wall region, and thus have different domain-wall energies. To study these domain walls, we initially prepare two single crystals of the same size: one with up polarization, the other with down polarization. We join these two structures and apply periodic boundary conditions, thereby forming two domains, separated from each other by two crystallographically identical (X or Y) 180° domain walls. We determine the zero-temperature equilibrium structure of each system by allowing all atoms to move to zero-force positions, thereby minimizing the total energy of the system. The simulations are performed under constant pressure conditions for both empirical and DFT calculations in order to capture the change in a volume as well as atomistic displacements. Both methods show less than 1% change in lattice parameters and volume from bulk ferroelectric values.

A. Domain-wall energy

Although the X walls and Y walls are defined to be parallel to the $(10\bar{1}0)$ and $(11\bar{2}0)$ planes, respectively, the actual position of the walls is not determined crystallographically but from minimization of the total energy of the system. The solid and dotted lines in Fig. 4(a) denote planes of high symmetry upon which the domain walls might be expected to lie. For the X walls, the two high-symmetry positions are along the ion planes and between the ion planes. For the Y walls, the three high-symmetry positions are at the cation plane, at the anion plane, and between two anion planes.

Both the empirical (E) and DFT calculations show that the equilibrium positions of the Y wall lies halfway between the anion planes. The calculations yield a Y wall energy of $E_{\mathrm{Y}}^{\mathrm{DFT}}=160$ mJ/m^2 and $E_{\mathrm{Y}}^{\mathrm{E}}=230$ mJ/m^2. That is, the domain-wall energy is defined by the difference in energies of a system with domain walls and a single crystal with the same number of ions, divided by the total area of domain wall in the system. The two methods also agree that the equilibrium position of the X wall lies equidistant between two ion planes, rather than at an ion plane. The X wall displays two different variants ($\mathrm{X_I}$ and $\mathrm{X_{II}}$) with very similar energies ($E_{\mathrm{X_I}}^{\mathrm{E}}=260$ and $E_{\mathrm{X_{II}}}^{\mathrm{E}}=255$ mJ/m^2) but different polarization profiles; the structural differences between these two variants and their origin will be discussed below. The DFT calculations show the same two different structural variants. However, it is not possible to uniquely partition the total energy in a DFT calculation among the various atoms; it is therefore not possible to determine the energies the two domain walls in the simulation cell separately. However, it is possible to extract the averaged energy value: $\frac{1}{2}(E_{\mathrm{X_I}}^{\mathrm{DFT}}+E_{\mathrm{X_{II}}}^{\mathrm{DFT}})=200$ mJ/m^2. Although, as is to be expected, the DFT and empirical values do not precisely agree, both methods do predict the Y walls to have a lower energy than the X walls. This conclusion is also consistent with the conclusions of Scrymgeour *et al.*[9] based on calculations using Ginzburg-Landau-Devonshire theory.

It is also possible to estimate the energy barriers for the motion of the domain walls by determining the energy of likely transition states. In particular, we can force the domain wall to be at a specific plane by setting the positions of the ions in the plane to be the average of the two opposite polarization states. For the Y wall, it seems logical that the cation plane should be the transition state because it is symmetric, lying halfway between two equivalent equilibrium positions. For this highly symmetric state, the empirical simulations yield an energy for the transition state of $E_{\mathrm{Y}}^{\mathrm{E*}}=485$ mJ/m^2, see Fig. 7, where the * superscript denotes the energy of the domain walls at the transition state. Assuming that this state is actually the transition state, the empirical calculations thus yield an energy barrier of 255 mJ/m^2, which is almost identical to the Y-wall energy itself. However, The DFT calculations yield an energy for the transition state of $E_{\mathrm{Y}}^{\mathrm{DFT*}}=285$ mJ/m^2, corresponding to an energy barrier of 125 mJ/m^2, which is only a half of the value obtained from the empirical calculations.

The transition states are slightly different for the two X-wall variants. The energies of the two X walls when centered at ion planes are calculated to be $E_{\mathrm{X_I}}^{\mathrm{E*}}=375$ mJ/m^2 and $E_{\mathrm{X_{II}}}^{\mathrm{E*}}=394$ mJ/m^2. Thus the estimated energy barrier for X-wall motion is 115 mJ/m^2 for the $\mathrm{X_I}$ wall and 140 mJ/m^2 for the $\mathrm{X_{II}}$ wall. The DFT calculations yield an average transition-state energy of $\frac{1}{2}(E_{\mathrm{X_I}}^{\mathrm{DFT*}}+E_{\mathrm{X_{II}}}^{\mathrm{DFT*}})=230$ mJ/m^2, corresponding to an average energy barrier of

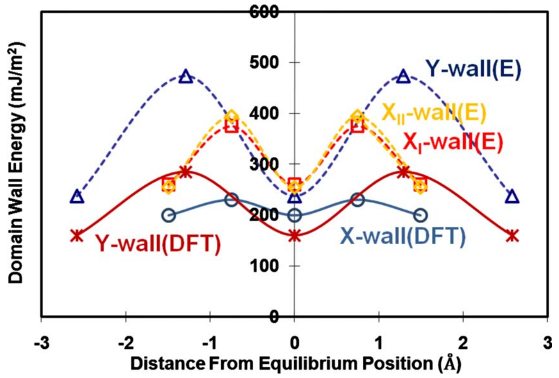

FIG. 7. (Color online) Energies of domain walls in equilibrium and in transition states. The equilibrium position is determined as equidistance between two anion planes for Y wall and center between the cation-anion mixed planes for X walls. The Y wall has a lower energy but higher-energy barrier for the wall motion than X wall. The lines are merely guides to the eye.

30 mJ/m^2. Again, there is a difference in the precise values from the empirical and DFT calculations; however, they both agree that the Y wall has a higher-energy barrier for domain-wall motion than the X walls.

B. Atomic displacement around domain walls

The domain walls break the crystallographic symmetry of the single crystal. Because of their proximity to two regions of opposite polarization, the atomic structure in the planes close to the domain walls should be a close approximation to the paraelectric structure, converging to the ferroelectric structure at some distance from the domain wall. Moreover, the domain walls produce displacements, not only parallel to the polarization direction (z), but also in the $x-y$ plane, with both components normal to and parallel to the domain wall. Following the notation of Scrymgeour *et al.*,[9] we denote displacements and polarizations normal to the domain wall as "normal" or "n," and those parallel to the domain wall (but orthogonal to the bulk uniaxial polarization) as "transverse" or "t." Close to the domain walls, all three components of polarization can be manifested.

1. *Y walls parallel to c-glide planes*

The Y wall lies between two anion planes separated by only 0.64 Å. The oxygen ion displacements in these planes are therefore large, as shown in Fig. 8. For the Y_1 domain wall, the O2 ions are closest to the domain-wall plane (~0.30 Å) and show the largest Z displacement from their ferroelectric positions, 0.23 Å. Because this displacement is almost as large as the displacement from the paraelectric to ferroelectric positions in bulk, we can understand this as the O2 ions moving back to positions close to their positions in the paraelectric phase. The next closest, O3 ion, is ~0.35 Å from the Y wall and shows a slightly smaller Z displacement of 0.21 Å. The O1 ion which sits further away yet, 0.65 Å, shows an even smaller Z displacement. The oxygen ion positions finally recover their bulk ferroelectric positions at a distance of ~5.8 Å away, as defined by the displacement from the ferroelectric positions dropping below 10% of its maximum value.

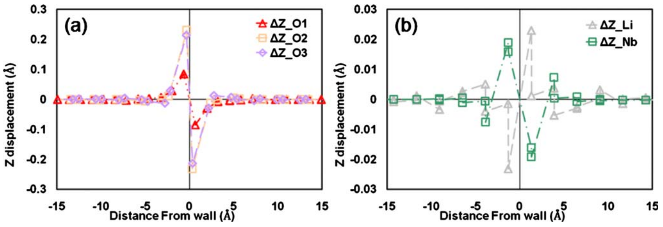

FIG. 8. (Color online) Displacement pattern relative to values in the bulk ferroelectric crystal in z direction of (a) oxygen ions and (b) cations around Y wall. Note the difference in scales of displacements.

Since at equilibrium the Y wall lies between two anion planes, the closest cation planes are much further away, 1.3 Å, and thus undergo significantly smaller Z displacements than the anions. Interestingly, the symmetries of the cations are also broken by the Y wall. However, in this case the symmetry breaking does not arise from the wall itself but as a secondary effect caused by the breaking of the symmetry of the O1, O2, and O3 ions. For example, the top Li in Fig. 6(c) is in an oxygen cage of different orientation than the oxygen cage enclosing the lower Li ion. Therefore, although they are the same distance from the Y wall, these two distinct $\mathrm{Li_I}$ and $\mathrm{Li_{II}}$ ions undergo different Z displacements (0.02 and 0.00 Å). Similarly, the distinct $\mathrm{Nb_I}$ and $\mathrm{Nb_{II}}$ ions also undergo Z different displacements (0.019 and 0.016 Å). The maximum cation displacements of both Nb and Li ion are, unsurprisingly, in the planes closest to the Y wall. These cation displacements are in the direction opposite to the displacements associated with the ferroelectricity, indicating that the cations are displaced back toward their paraelectric positions. The cations recover their ferroelectric positions ~11.7 Å from the wall, which is twice the distance of that required by the anions.

Because the oxygen ions near the Y wall shift oppositely poled ferroelectric states to approximately paraelectric symmetric position at the domain walls, the oxygen ions on opposite sides of the domain wall displace in opposite transverse directions. If an oxygen ion moves along the positive y axis along on one side of the wall, the crystallographically equivalent oxygen ion on the opposite side moves along the negative y axis. For displacements normal to the wall, symmetric oxygen ions on opposite sides displace equally either toward or away from the Y wall regardless of ferroelectric state. Figures 9(a) and 9(b) shows the transverse and normal displacements of the oxygen ions in the region around a Y wall; Figs. 9(c) and 9(d) show the corresponding displacements for the cations. Here, the positive and negative signs of the transverse displacement correspond to movement in the $+y$ and $-y$ directions. Figure 9(c) shows the transverse displacements of cations at the nearest cation plane of the up-polarized region; the transverse displacements for the down polarization side are equal and opposite. For normal displacements, the positive and negative signs denote displacement movement away from and toward the Y wall, respectively.

The transverse displacements of the three different nonsymmetric oxygen ions can be analyzed in a similar manner.

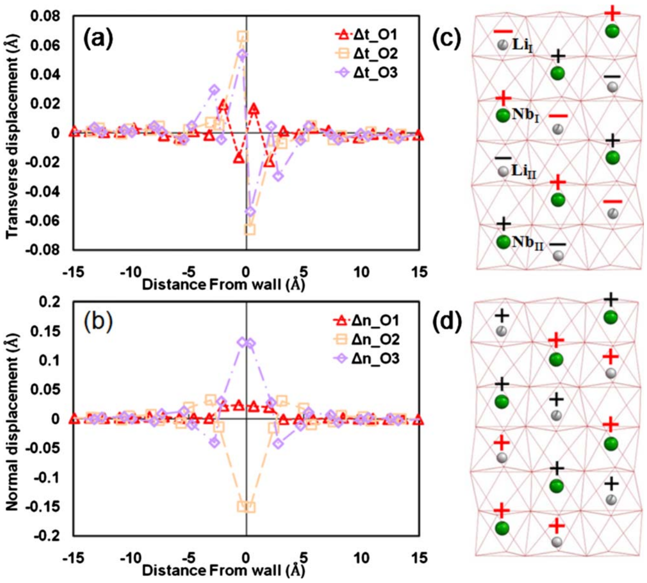

FIG. 9. (Color online) Atomic displacements of O1, O2, and O3 ions relative to the bulk ferroelectric phase in (a) transverse and (b) normal direction directions near a Y wall. Schematic view of corresponding cation displacements along (c) transverse and (d) normal directions. Relative larger+signs (red) and smaller+signs (black) represent larger and smaller cation displacements. For transverse displacements, the plus and minus sign indicate the positive and negative displacement along Y_1 axis. For normal displacement, the plus sign indicates that the cation moves away from the Y wall while the minus sign designates that cation displaces toward Y wall.

As Fig. 9(a) shows the O1, O2, and O3 ions on the one side of the wall displace in opposite directions from their counterparts on the other. Because the closest anion to the wall, O2, shows the largest displacement in z direction, it also has the largest transverse displacement, $O2_T \sim 0.066$ Å.

As we can see from Fig. 9(b), the normal displacements of oxygen ions show the same pattern on the two sides of the domain wall. For the Y_1 axis, the O1 ions have same x positions, but different y positions in the two different ferroelectric states; they thus displace along only in the transverse direction. Specifically, the simulations show that the Y wall pushes the O1 ion away from the wall; the normal displacement is $O1_N \sim 0.02$ Å at the nearest oxygen plane.

The normal displacements of the O2 and O3 ions are almost equal and opposite to each other ($O2_N \sim -0.15$ Å and $O3_N \sim 0.13$ Å) because the Y_2 and Y_3 axes are oriented at −60° and +60° angle to the Y wall. These displacements are larger than the ferroelectrics displacements, ±0.11 Å, resulting in additional normal displacements of oxygen ions which break the paraelectric symmetries of oxygen ions near the Y wall.

The broken symmetry of the oxygen ions also causes the cations to break the uniaxial symmetry around the Y wall. Figures 9(c) and 9(d) show schematic views of the transverse and normal cation displacements for the cation plane closest to the Y wall, at which the displacements are largest. The Li_I and Nb_I show relatively larger transverse displacements than the Li_{II} and Nb_{II} ions. As we can see from Fig. 9(c), the Li and Nb ions displace in opposite transverse direction, although Li_I and Li_{II} ions displace in same transverse directions, as do the two types of Nb ions. Figure 9(d) shows that all of the cations near Y wall are displaced in the normal direction away from Y wall. Because of their weaker electrostatic interactions with the oxygen ions, the Li ions displace more than the Nb ions. Because of the differences in the symmetries of the displacement pattern along the transverse and normal direction, the normal displacements of cations converge to zero at relatively longer distances from the Y wall (∼11.67 Å) than the transverse displacement (∼6.48 Å).

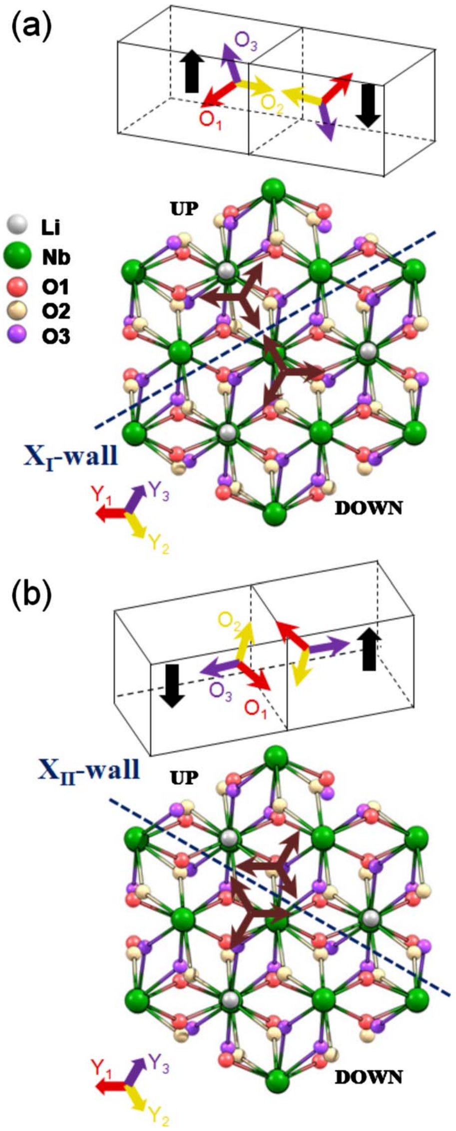

FIG. 10. (Color online) Crystallographies of the X_I wall and X_{II} wall.

2. X walls perpendicular to c-glide plane

The structure of the X wall is very different from that of the Y wall for two reasons. Most importantly, the X wall lies parallel to planes that contain both anions and cations. More subtly, because it lies at 30° to the Y wall, the X wall is normal to one of the Y directions, and at ±30° to the other

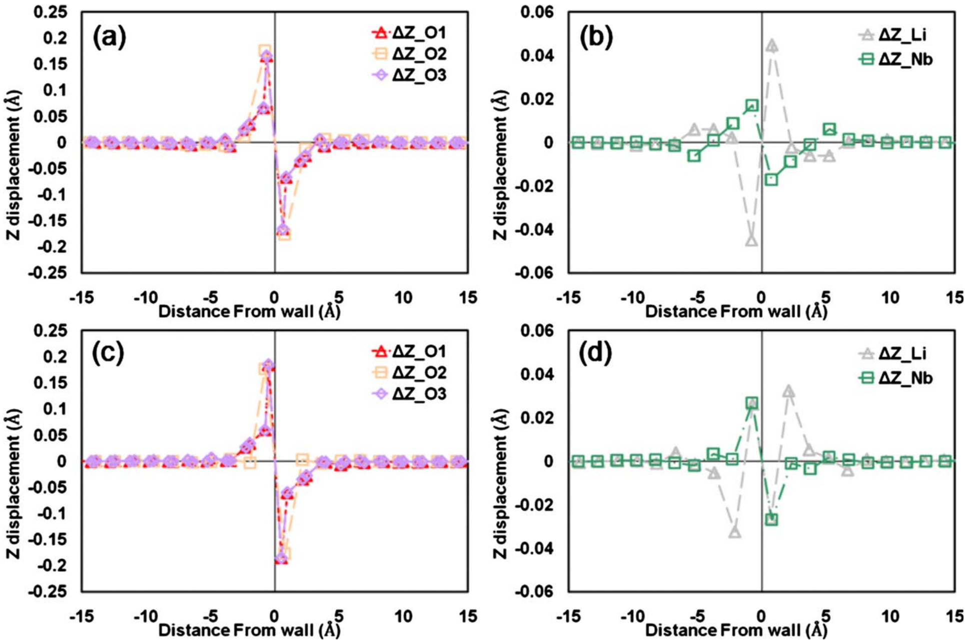

FIG. 11. (Color online) The *Z*-displacements patterns relative to the bulk ferroelectric phase around X_I wall and X_{II} wall. (a) The anion displacement pattern around X_I wall. (b) The cation displacement pattern around X_I wall. (c) The anion displacement pattern around X_{II} wall. (d) The cation displacement pattern around X_{II} wall.

two. Because of the differing oxygen displacements on the oxygen sublattices, this creates two X-wall variants, depending on whether the other oxygen displacements point into the X wall or point out of the X wall. In particular, as Fig. 10(a) shows, when the Y_2 direction is perpendicular to the X walls, the O2 ions mainly displace in the normal direction into the domain wall, leading to the X_I wall. An O2 ion sitting near the X_I wall moves in the $+Y_2$ direction for the up polarization and in the $-Y_2$ direction for the down polarization state. Both of these displacements represent normal displacements toward the X_I wall. Likewise, Fig. 10(b) shows that when the Y_3 direction is perpendicular to the X wall, the O3 ions displace along the normal direction away from the domain wall. This direction is opposite to that for X_I wall, thus creating a different variant, the X_{II} wall. The positive displacement of the O3 ion along Y_3 axis near the X_{II} wall for up polarization and negative displacement for down polarization indicates the movement of O3 ions away from the X_{II} wall.

Figures 11(a) and 11(b) show the displacement patterns of the anions and cations in the *Z* direction around the X_I wall. The *Z* displacement is largest in the planes closest to the domain wall, decaying to zero at ~5 Å from the wall. The corresponding cation displacements are much smaller with the cations moving closer to their paraelectric positions. Figures 11(c) and 11(d) show the anion and cation displacements around the X_{II} wall. The *Z* displacements of the oxygen ions are quite similar for the two X-wall variants, except that the maximum *Z* displacement of the X_{II} wall is slightly larger (0.19 vs 0.17 Å). However, comparing Figs. 11(b) and 11(d), there are significant differences in the cation displacements. For the X_I wall, the maximum *Z* displacement of both cations is observed at the nearest plane. For the X_{II} wall, the Li and Nb ions move by the same amount in the *Z* direction at the closest plane, thereby compensating for the displacement of oxygen positions in the *Z* direction. As a result, the Li ion closest to its paraelectric position is at the second-nearest plane. In contrast to the Y walls, there is only one type of *Z*-displacement pattern for Li ion and Nb ion in the X walls

The two X-wall variants also create two distinct patterns of normal and transverse ion displacements, see Fig. 12(a). The negative sign in the normal displacement for the O2 ions indicates that they move toward the X_I wall; the O1 and O3 ions move away from X_I wall by equal amounts along their internal *Y* axes. In a similar manner, Fig. 12(b) shows the displacements of the anions near X_{II} wall. The maximum normal displacement (~0.17 Å) at the plane closest to the wall disappears ~5 Å away from both of X walls. Figure 12(c) shows the transverse displacement of the anions around the X_I wall; the displacements for the X_{II} wall are very similar. All of the transverse displacements of the anions are cancelled by equal and opposite displacement patterns. The displacement of cations around the two X walls are shown in Fig. 12(d) through Fig. 12(f). Unlike the Y wall, only one normal displacement pattern for each cation is observed for both X walls. Figure 12(d) shows the cation displacement around the X_I wall. The first +/− sign for each cation represents the normal displacement while the second +/− sign designates the transverse displacement of the cations. The Li and Nb ions, which move in opposite normal direction, show the largest displacement at the second-nearest plane from X_I wall. Both Li and Nb ions in the first plane move away from the X_{II} wall, Fig. 12(e). However, the Li ions in the second plane move into the X_{II} wall while the Nb ions shift away, Fig. 12(f). The transverse displacement of the cations are very similar to the anion displacement. Unlike the normal and *Z* displacement pattern of cations, the nonsymmetric cations, Li_I, Li_{II} and Nb_I, Nb_{II}, show opposite displacements in the transverse direction. Therefore, the equal and opposite transverse displacement of each cation along *Z* direction will be cancelled out.

C. Polarization at domain walls

The switching of the polarization at a ferroelectric domain wall is generally considered to be relatively abrupt, taking

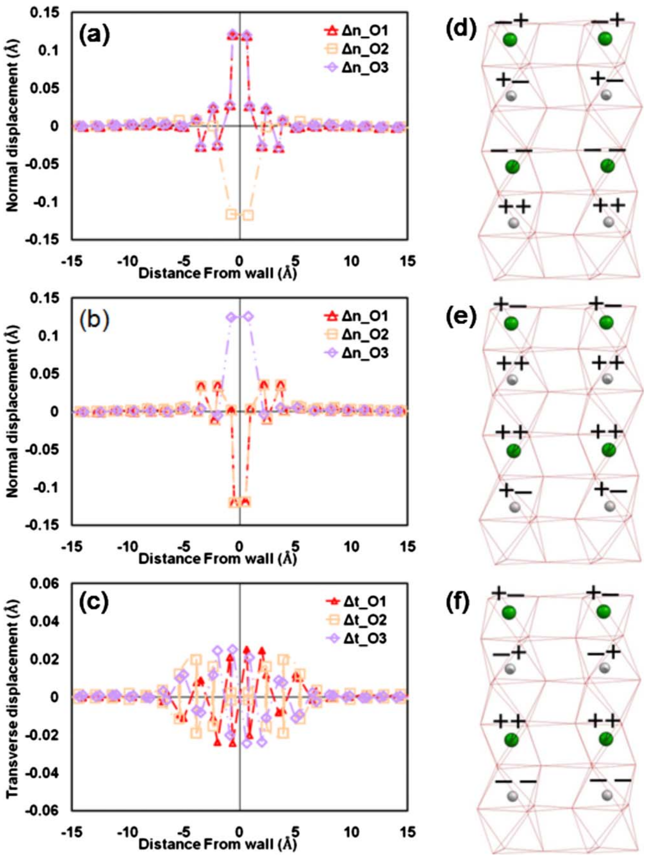

FIG. 12. (Color online) Normal displacements of three different oxygen ions relative to the bulk ferroelectric phase near (a) $X_{\rm I}$ wall and (b) $X_{\rm II}$ wall. (c) Transverse displacements of three different oxygen ions around $X_{\rm I}$ wall. (d) Normal and transverse displacement of cations around $X_{\rm I}$ wall. Normal displacement of cations around $X_{\rm II}$ wall at (e) the nearest and (f) the second-nearest plane.

place over only one or two unit cells.[33] However, the relatively long distances (up to ~10 Å) over which the atomic displacements return to bulk values suggest that the polarization may be governed by a similar length scale. In this section, we characterize the transition in the uniaxial polarization, and in the components of polarization normal to and transverse to the domain wall. As we shall see, these more complex polarization patterns manifest some features reminiscent of those present in ferromagnetic domain walls in which the spin state switches from one to another over, typically, many tens of unit cells.[34] However, because of the much greater strength of electrostrictive interactions compared to magnetostrictive interactions, the nonuniaxial components are relatively small and characterized by shorter length scales than their magnetic counterparts.

1. Y wall

We have determined the polarization along the direction normal to the Y wall using both empirical potentials and DFT. As is customary,[35] for the DFT calculation both ionic and electronic contributions to the polarization are considered by implementing the Born effective charge (BEC) formalism. The BEC analysis, developed by Veithen and Ghosez[27] and using the Berry phase approach, was used to analyze the bulk $\mathrm{LiNbO_3}$ ferroelectric system. As Fig. 13(a) shows, the two methods give very similar profiles in the uniaxial contribution to the polarization. The asymmetric pattern of up and down polarization arises from the shift in the Y wall from the anion plane to the equilibrium positions; as a result, one of the domains is wider than the other. We note that using the full ionic charge in analyzing the DFT results, rather than the Born effective charges, leads to almost complete overlap with the polarization profiles determined from the empirical potentials. We take the good agreement between the DFT and empirical results as validation for the larger scale calculations using the empirical potentials, which show a change in P_z over a very short distance, see Fig. 13(b).

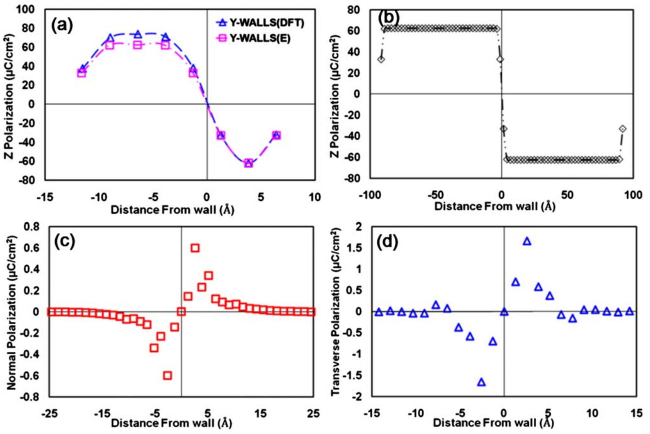

FIG. 13. (Color online) (a) Comparison of z-directional polarization (P_z) around Y walls, determined by DFT and empirical simulation methods. (b) Uniaxial polarization profile of larger simulation cell with Y wall. Variation in in-plane polarization near Y wall; (c) normal and (d) transverse. Polarization profile at each side of Y wall shows exactly antisymmetric behavior.

The nonuniaxial displacements of the ions generate nonuniaxial contributions to the polarization. Figure 13 shows (c) the normal and (d) the transverse polarization around the Y wall. Both are antisymmetric around the domain wall with zero polarization contributions at the center of domain wall. The normal and transverse polarizations show maximum values of 0.60 and 1.66 $\mu\mathrm{C/cm^2}$ at 2.58 Å, decaying to zero ~9 Å away from the wall.

A 180° ferroelectric wall is typically understood as Ising type; by contrast a 180° magnetic wall is typically understood as Bloch type or Néel type.[36] The presence of significant polarization components P_n and P_t of up to ~2.66% of P_z gives rise to a Bloch-type and a Néel-type contribution to the predominantly Ising-type Y wall.[37] The polarization vector, $\boldsymbol{P_z}+\boldsymbol{P_t}$ leads to a Bloch-type rotation by angle θ_B in the t-z plane of the domain wall, Fig. 14(b), whereas polarization vector, $\boldsymbol{P_z}+\boldsymbol{P_n}$ leads to a Néel-type rotation by angle θ_N in the n-z plane perpendicular to the domain wall, Fig. 14(c). The maximum rotation angles of $\theta_B \sim 1.52°$ and $\theta_N \sim 0.55°$ occur at a distance $x_n \sim \pm 1.3$ Å from the Y wall where the P_n and P_t components are maximum. Thus the Y wall has a relatively strong Bloch-type rotation behavior and a weak Néel-type rotation behavior.

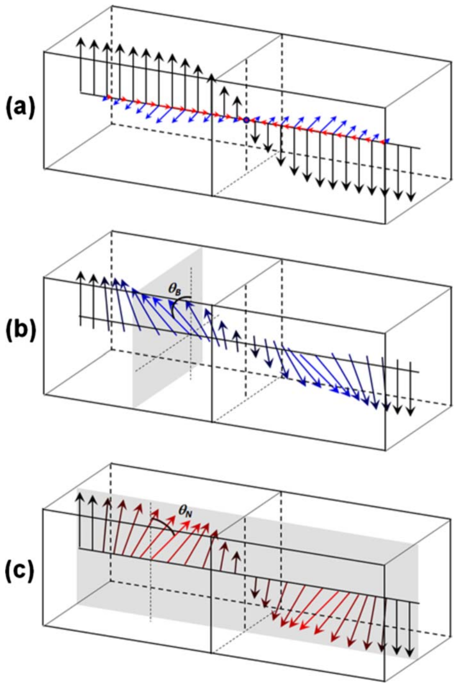

FIG. 14. (Color online) Schematic representation of (a) three different polarization, P_z, P_t, and P_n; (b) Bloch-type wall is created by vector sum of P_z and P_t and (c) Néel-type wall is created by vector sum of P_z and P_n. θ_B and θ_N is calculated by maximum rotation angle of polarization at the position where P_z returns to bulk polarization value.

2. X walls

As in the case of the Y wall, the empirical and DFT calculations yield very similar polarization patterns around the X walls, see Fig. 15(a). To understand the polarization pattern around the X walls without the limitations of small system sizes, we again perform larger scale simulations with the empirical potentials. For the geometry used in this study, the X_I wall lies at center of the system, while the X_{II} wall lies on the periodic boundary at ±70 Å. As we can see from the figure, both X walls show very sharp transition regions between polarization states. The bulk polarization of 62.4 $\mu C/cm^2$ is reached at ~6 Å away from X_I wall and at ~9 Å away from X_{II} wall.

Because the atomic displacements in the transverse direction are cancelled by equal and opposite movement of each ion, Fig. 12(c), there are no transverse polarizations at the X walls. Figures 15(c) and 15(d) show the normal polarization profile around X_I wall and X_{II} wall, respectively. The different normal polarization patterns near the two X walls are the result of different displacements of the cations. With the largest normal displacements at the second-nearest plane, the maximum polarization of 0.61 $\mu C/cm^2$ out of X_I wall is observed at 5.2 Å away, slowly decreases in a monotonic manner, reaching 10% of its maximum value about ~15 Å away. The change in normal displacement pattern of cations between the first- and second-nearest plane to X_{II} wall generates the maximum outward polarization of 0.71 $\mu C/cm^2$ at 1.49 Å and leads to oscillatory convergence over a distance of ~9 Å. Considering the maximum Bloch-type and Néel-type rotation angles near the X walls, the angles are $\theta_B \sim 0°$ and $\theta_N \sim 0.56°$ for the X_I wall and $\theta_B \sim 0°$ and $\theta_N \sim 0.65°$ for the X_{II} wall. Thus, both X walls show only Néel-type rotation.

D. Domain-wall width

The Ginzburg-Landau-Devonshire (GLD) (Refs. 38–40) thermodynamic theory successfully explains the relationship between the variation in the polarization and domain-wall width in the transition region for both perovskite materials[39] and for trigonal ferroelectrics such as $LiNbO_3$ and $LiTaO_3$.[9] In the transition region, the total free energy of a ferroelectric material can be understood as arising from four different

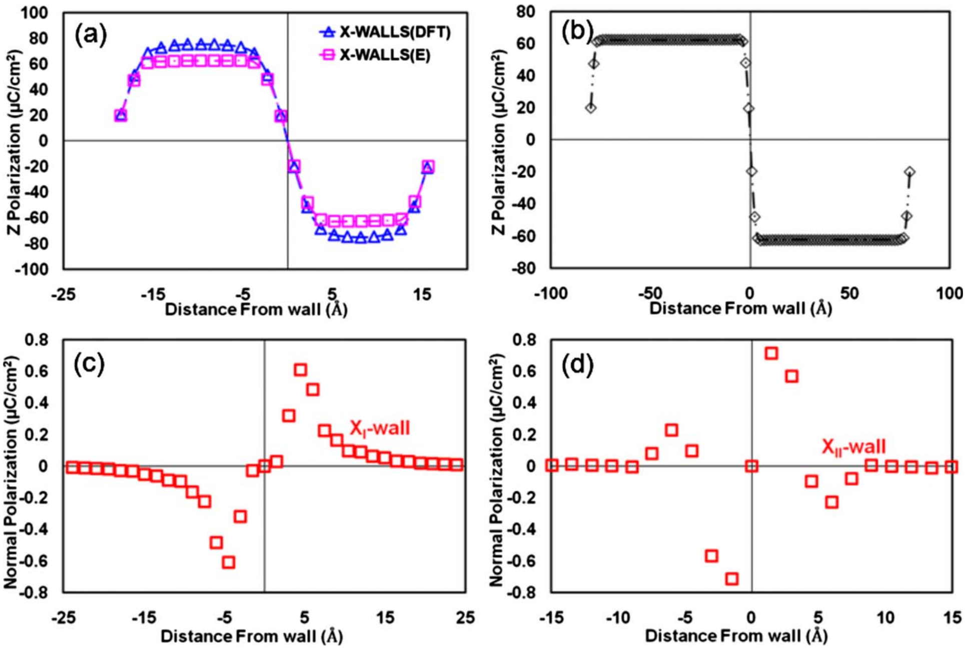

FIG. 15. (Color online) (a) Comparison on Z directional polarization around X walls between DFT and empirical simulation methods. (b) Uniaxial polarization profile of larger simulation cell with X walls. Two different X walls are created at the center (X_I wall) and at the boundary (X_{II} wall). (c) The variation in in-plane polarization around X walls; normal polarization profile near (c) X_I wall and (d) X_{II} wall.

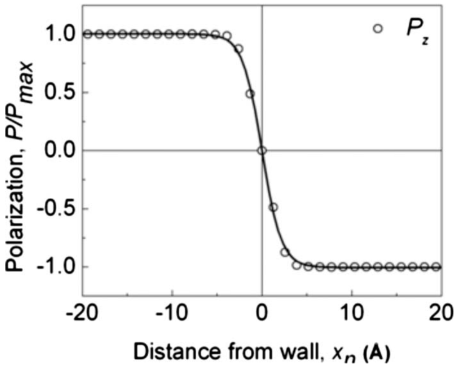

FIG. 16. A fit of P_z to hypertangent function around Y wall. Equation (5) yields the domain-wall width $\omega_o \sim 2.16 \pm 0.05$ Å.

energy components:[41,42] a free energy associated with the second-order phase transition, a free energy associated with elastic lattice displacement, a free energy derived from structural distortion by nonuniform polarization, and a free energy association with the gradient in polarization.

Solving the free-energy equation for energy minima, Scrymgeour *et al.*,[9] show the relationship between three components of polarizations, P_n, P_t, and P_z as

$$P_z(x_n) = P_0 \tanh\left(\frac{x_n}{\omega_0}\right) \quad (5)$$

and

$$\begin{bmatrix} P_n(x_n) \\ P_t(x_n) \\ P_z(x_n) \end{bmatrix} = \begin{bmatrix} \rho_{n1} & \rho_{n2} & \rho_{n3} \\ \rho_{t1} & \rho_{t2} & \rho_{t3} \\ 1 & 0 & 0 \end{bmatrix} \times \begin{bmatrix} P_z \\ P_z^3 \\ P_z^5 \end{bmatrix}, \quad (6)$$

where, ρ_{ik} ($i=n,t$; $k=1,2,3$) are the coefficients of the polynomials.

Our atomic-scale simulation study also shows that nonuniaxial polarizations are strongly correlated with the uniaxial polarization. While P_z shows a kink-type polarization variation reaching zero at the center of the wall, P_n and P_t are zero both at the center of the wall and far away from the wall. The simulations discussed above show that in-plane polarizations reach their maximum value at approximately the same distance from the domain wall as P_z returns to bulk value. Thus, P_n and P_t returns to zero bulk value at relatively longer distance than P_z. Because, no complete model has been developed for the nonuniaxial polarizations of trigonal systems, we only show the domain wall half width along with P_z component in this study. A fit of P_z to a single hyperbolic function, Eq. (5), yields $\omega_o \sim 2.16 \pm 0.05$ Å. Figure 16 show normalized polarization profiles of P_z along x_n around the Y wall. The solid line is a fit to simulation results for P_z.

The two X walls yield essentially identical domain wall half width: $\omega_o \sim 2.10 \pm 0.03$ Å for the X_I wall and $\omega_o \sim 2.12 \pm 0.03$ Å for the X_{II} wall, as shown in Fig. 17. The fits of P_z to single hyperbolic function lead to very similar domain wall half width for three different types of domain walls. The absence of analytic results for nonuniaxial contributions to the polarization indicates that there is still scope for further developments in the GLD analysis of these domain walls.

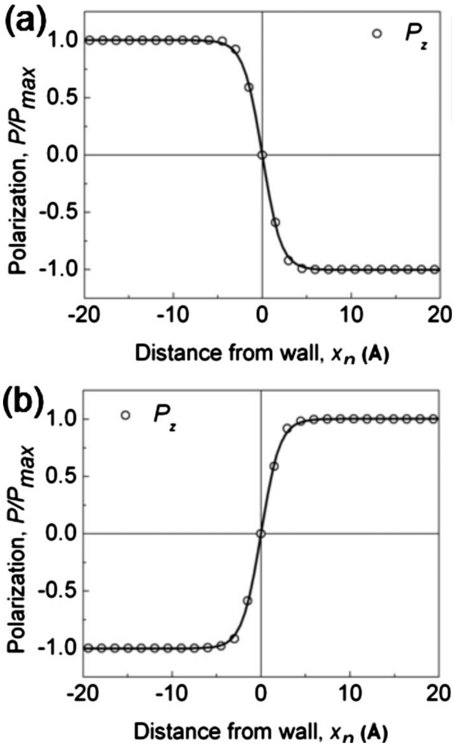

FIG. 17. Fits of P_z of (a) X_I wall and (b) X_{II} wall to Eq. (5). The fits of P_z yield almost same pattern between Y wall and two X walls. Further analysis on in-plane polarization is required for the comparison.

E. Threshold field for domain-wall motion

Ishibashi[43] and Suzuki[44] showed that the width of the domain wall controls domain-wall motion with the activation energy for wall motion being inversely proportional to its width. In their analysis, the activation energy for domain-wall motion, can be expressed as a free-energy difference between equilibrium state and transition state, $\Delta F_{activation}$,

$$\Delta F_{activation} = F_{Transition} - F_{Equilibrium} \approx \alpha_1 P_s^2 \omega_0 \left(\frac{\omega_o}{a}\right)^3 \times e^4 \left(\frac{\pi}{2}\right)^{7/2} \exp\left(-\frac{\pi^2 \omega_o}{a}\right), \quad (7)$$

where α_1 and α_2 are the constant in the GLD polynomial, ω_0 is domain-wall half width, P_S is spontaneous polarization, and a is lattice constant. From this the threshold field for domain-wall motion can be determined as the activation energy dividing by $\omega_0 P_S$.[45]

In the previous section, we obtained domain-wall widths by fitting the P_z profiles. The lattice parameter for Y wall shows $a \sim 5.1684$ Å and spontaneous polarization $P_S \sim 62.4$ μC/cm^2. The coefficients for the GLD polynomial constants can be determined from the polarization and Curie-Weiss law,

TABLE II. Comparison on constants in Eq. (7).

Parameters	This works	Literature[a]	Units
a	5.1684	5.1474	$\times 10^{-10}$ m
α_1	5.04	2.012	$\times 10^9$ Nm^2/C^2
α_2	12.95	3.608	$\times 10^9$ Nm^6/C^4
P_s	62.4	75	μC/cm^2

[a] Reference 9.

$$P_s = \sqrt{\frac{\alpha_1}{\alpha_2}} \quad \text{and} \quad \alpha_1 = \frac{1}{\varepsilon_r - 1}. \tag{8}$$

The comparison between the calculated constant values and literature value for the parameters entering Eq. (7) is listed in Table II. Using Table II and Eq. (7), we obtain the activation energy and threshold field for the different domain walls. Because the three domain walls have essentially identical widths, Eq. (7) yields almost the same value in activation energy and threshold field. The calculated activation energies are $\Delta F_{acti} \sim 133$ mJ/m^2 and $E_{th} \sim 1.0 \times 10^9$ V/m with the GLD parameters calculated, and 77 mJ/m^2 and $E_{th} \sim 5.0 \times 10^8$ V/m with the constants from the literature. These are comparable to the estimates from the atomistic simulations of $\Delta F_{acti}^{\mathrm{MD}} \sim 255$ mJ/m^2 and $\Delta F_{acti}^{\mathrm{DFT}} \sim 125$ mJ/m^2 for Y wall, and $\Delta F_{acti}^{\mathrm{MD}} \sim 115$ mJ/m^2 for X$_\mathrm{I}$ wall and 140 mJ/m^2 for X$_\mathrm{II}$ wall and $\Delta F_{acti}^{\mathrm{DFT}} \sim 30$ mJ/m^2 for an average value of two X walls. Because P_z yields essentially the same domain-wall width for all three domain walls, the threshold fields are similar. However, the normal and parallel polarization contributions are different in each case, which could have a significant effect on the threshold field. In the absence of a theory of these nonuniaxial polarizations for the trigonal structure, we cannot estimate their effect, however. Thus further development of the model for the nonuniaxial component of polarization is necessary to improve the GLD phenomenological analysis.

V. CONCLUSIONS AND DISCUSSION

The structure and energetics of domain walls in LiNbO$_3$ have been studied by empirical potentials and verified by DFT. The Y wall is energetically favored but should be less mobile because the activation energy for migration is higher. The broken symmetries of both cations and anions near the wall lead to nonuniaxial polarization. This expands the characteristics of ferroelectric domain wall from simple Ising-type to include Bloch-type and Néel-type components. The fits to the GLD formalism of uniaxial polarization profiles of different domain walls lead to very similar domain-wall widths. Although the absolute value of the in-plane polarization is small, less than 3% of uniaxial polarization, the in-plane polarization has an important role for understanding ferroelectric domain-wall behavior in LiNbO$_3$. Moreover, since other material systems also appear to show such in-plane wall components,[37] it is possible that mixed Bloch-type and Néel-type character to ferroelectric walls may be more ubiquitous. These nonuniaxial polarization components can change the relative electrostatic energies of different wall orientations and can explain why some wall orientations are seen and not the others.[9]

ACKNOWLEDGMENTS

We are grateful to Anna Morozovska for useful discussions. This work was supported by the National Science Foundation under Grants No. DMR-0602986 and No. DMR-0303279. The computation resources are provided by the High Performance Center (HPC) at University of Florida and Florida Laboratory for Advanced Materials Engineering Simulation (FLAMES).

---

*Corresponding author; sphil@mse.ufl.edu

[1] K. K. Wong, *Properties of Lithium Niobate* (INSPEC, The Institution of Electrical Engineers, London, United Kingdom, 2002).

[2] A. M. Prokhorov and Y. S. Kuz'minov, *Physics and Chemistry of Crystalline Lithium Niobate* (Taylor & Francis, London, 1990).

[3] L. Arizmendi, Phys. Status Solidi A **201**, 253 (2004).

[4] V. Gopalan, M. J. Kawas, M. C. Gupta, T. E. Schlesinger, and D. D. Stancil, IEEE Photon. Technol. Lett. **8**, 1704 (1996).

[5] V. Soluch and M. Lysakowska, IEEE Trans. Ultrason. Ferroelectr. Freq. Control **52**, 145 (2005).

[6] H. Landolt and R. Börnstein, *Numerical Data and Functional Relations in Science and Technology* (Springer, Berlin, 1981).

[7] S. R. Phillpot and V. Gopalan, Appl. Phys. Lett. **84**, 1916 (2004).

[8] V. Gopalan, V. Dierolf, and D. A. Scrymgeour, Annu. Rev. Mater. Res. **37**, 449 (2007).

[9] D. A. Scrymgeour, V. Gopalan, A. Itagi, A. Saxena, and P. J. Swart, Phys. Rev. B **71**, 184110 (2005).

[10] W. Kohn and L. J. Sham, Phys. Rev. **140**, A1133 (1965).

[11] R. G. Parr and W. Yang, *Density-Functional Theory of Atoms and Molecules* (Oxford University Press, New York, 1989).

[12] G. Kresse and J. Furthmuller, Comput. Mater. Sci. **6**, 15 (1996).

[13] G. Kresse and J. Furthmuller, Phys. Rev. B **54**, 11169 (1996).

[14] P. E. Blöchl, Phys. Rev. B **50**, 17953 (1994).

[15] J. P. Perdew and W. Yue, Phys. Rev. B **33**, 8800 (1986).

[16] Q. K. Li, B. Wang, C. H. Woo, H. Wang, and R. Wang, J. Phys. Chem. Solids **68**, 1336 (2007).

[17] M. P. Teter, M. C. Payne, and D. C. Allan, Phys. Rev. B **40**, 12255 (1989).

[18] P. Pulay, Chem. Phys. Lett. **73**, 393 (1980).

[19] H. X. Xu, D. Lee, J. He, S. B. Sinnott, V. Gopalan, V. Dierolf, and S. R. Phillpot, Phys. Rev. B **78**, 174103 (2008).

[20] R. A. Jackson and M. E. G. Valerio, J. Phys.: Condens. Matter **17**, 837 (2005).

[21] D. Wolf, P. Keblinski, S. R. Phillpot, and J. Eggebrecht, J. Chem. Phys. **110**, 8254 (1999).

[22] H. Donnerberg, S. M. Tomlinson, C. R. A. Catlow, and O. F.

Schirmer, Phys. Rev. B **40**, 11909 (1989).

[23] P. Paufler, Acta Crystallogr., Sect. A: Found. Crystallogr. **63**, 483 (2007).

[24] H. Boysen and F. Altorfer, Acta Crystallogr., Sect. B: Struct. Sci. **50**, 405 (1994).

[25] K. Parlinski, Z. Q. Li, and Y. Kawazoe, Phys. Rev. B **61**, 272 (2000).

[26] A. V. Postnikov, V. Caciuc, and G. Borstel, J. Phys. Chem. Solids **61**, 295 (2000).

[27] M. Veithen and P. Ghosez, Phys. Rev. B **65**, 214302 (2002).

[28] S. C. Abrahams, J. M. Reddy, and J. L. Bernstein, J. Phys. Chem. Solids **27**, 997 (1966).

[29] H. D. Megaw, Acta Crystallogr., Sect. A: Cryst. Phys., Diffr., Theor. Gen. Crystallogr. **24**, 583 (1968).

[30] S. C. Abrahams, H. J. Levinstein, and J. M. Reddy, J. Phys. Chem. Solids **27**, 1019 (1966).

[31] A. M. Glazer, Acta Crystallogr., Sect. A: Cryst. Phys., Diffr., Theor. Gen. Crystallogr. **31**, 756 (1975).

[32] H. D. Megaw, *Crystal Structures: A Working Approach* (W. B. Saunders, Philadelphia, 1973).

[33] J. Padilla, W. Zhong, and D. Vanderbilt, Phys. Rev. B **53**, R5969 (1996).

[34] A. Goldman, *The Handbook of Modern Ferromagnetic Materials* (Springer, New York, 1999).

[35] B. Meyer and D. Vanderbilt, Phys. Rev. B **65**, 104111 (2002).

[36] K. C. Kao, *Dielectric Phenomena in Solids* (Academic Press, New York, 2004).

[37] D. Lee, R. K. Behera, P. Wu, H. Xu, Y. L. Li, S. B. Sinnott, S. R. Phillpot, L. Q. Chen, and V. Gopalan, Phys. Rev. B **80**, 060102(R) (2009).

[38] A. F. Devonshire, Philos. Mag. **42**, 1065 (1951).

[39] V. A. Zhirnov, Zh. Eksp. Teor. Fiz. **35**, 1175 (1958) [Sov. Phys. JETP **8**, 822 (1959)].

[40] V. L. Ginzburg, Fiz. Tverd. Tela (Leningrad) **2**, 2031 (1960) [Sov. Phys. Solid State **2**, 1824 (1961)].

[41] F. Jona and G. Shirane, *Ferroelectric Crystals* (Pergamon Press, Oxford, 1962).

[42] L. N. Bulaevskii, Fiz. Tverd. Tela (St. Petersburg) **5**, 3183 (1963) [Sov. Phys. Solid State **5**, 2329 (1964)].

[43] Y. Ishibashi, J. Phys. Soc. Jpn. **46**, 1254 (1979).

[44] Y. Ishibashi and I. Suzuki, J. Phys. Soc. Jpn. **53**, 1093 (1984).

[45] S. Choudhury *et al.*, J. Appl. Phys. **104**, 084107 (2008).